

Observation of three-photon bound states in a quantum nonlinear medium

Qi-Yu Liang,¹ Aditya V. Venkatramani,² Sergio H. Cantu,¹ Travis L. Nicholson,¹ Michael J. Gullans,³ Alexey V. Gorshkov,³ Jeff D. Thompson,⁴ Cheng Chin,⁵ Mikhail D. Lukin,² and Vladan Vuletić¹

¹*Department of Physics and Research Laboratory of Electronics,
Massachusetts Institute of Technology,
Cambridge, Massachusetts 02139, USA*

²*Department of Physics, Harvard University,
Cambridge, Massachusetts 02138, USA*

³*Joint Quantum Institute and Joint Center for Quantum Information and Computer Science,
National Institute of Standards and Technology and
University of Maryland, College Park, Maryland 20742, USA*

⁴*Department of Electrical Engineering,
Princeton University, Princeton, NJ 08544, USA*

⁵*James Franck Institute, Enrico Fermi Institute and Department of Physics,
University of Chicago, Chicago, IL 60637, USA*

(Dated: December 14, 2024)

Bound states of massive particles, such as nuclei, atoms or molecules, are ubiquitous in nature and constitute the bulk of the visible world around us. In contrast, photons typically only weakly influence each other due to their very weak interactions and vanishing mass. We report the observation of traveling three-photon bound states in a quantum nonlinear medium where the interactions between photons are mediated by atomic Rydberg states. In particular, photon correlation and conditional phase measurements reveal the distinct features associated with three-photon and two-photon bound states. Such photonic trimers and dimers can be viewed as quantum solitons with shape-preserving wavefunctions that depend on the constituent photon number. The observed bunching and strongly nonlinear optical phase are quantitatively described by an effective field theory (EFT) of Rydberg-induced photon-photon interactions, which demonstrates the presence of a substantial effective three-body force between the photons. These observations pave the way towards the realization, studies, and control of strongly interacting quantum many-body states of light.

Bound states of light quanta have been proposed to exist in specifically engineered media with strong optical nonlinearities [1–4]. Recently photonic dimers have been observed experimentally [5]. Such bound states of photons can be viewed as quantum solitons [6, 7], which are shape-preserving wave-packets enabled by the cancellation of nonlinear and dispersive effects. In contrast to classical solitons where the self-consistent shape varies smoothly with total pulse energy, in a quantum soliton the optical nonlinearity is so strong that the wave packet shape depends on the constituent number of photons in a quantized manner [6, 7]. The creation of quantum solitons not only represents an important step in fundamental studies of photonic quantum matter [5, 8, 9], but also may enable new applications in areas ranging from quantum communication to quantum metrology [10, 11].

We search for a photonic trimer using an ultracold atomic gas as a quantum nonlinear medium. This medium is experimentally realized by coupling photons to highly excited atomic Rydberg states by means of electromagnetically induced transparency (EIT). The resulting hybrid excitations of light and matter – Rydberg polaritons – inherit strong interactions from their Rydberg components, and can propagate with very low loss at slow group velocity v_g [12–14]. The nonlinearity arises when photons are within a Rydberg blockade radius r_B of one another, where strong interactions between atoms in the Rydberg state [15] shift the Rydberg level out of the EIT resonance, blocking the excitation of more than one Rydberg atom within r_B . In the dissipative regime (on atomic resonance), the blockade results in photon loss and anti-bunching [16–18]. In the dispersive, off-resonant regime, the index of refraction varies with the separation between photons, resulting in an attractive force [5].

Our experimental setup is illustrated in Figs. 1A,B, and has been described previously [19]. In brief, a weak quantum probe field at 780 nm is coupled to the $100S_{1/2}$ Rydberg state via a strong 479 nm control field in the EIT configuration (see Fig. 1B). The interactions occur in a cloud of laser-cooled ^{87}Rb atoms in a far-detuned optical dipole trap. The system

is effectively one-dimensional for the photons, since the blockade radius ($r_B = 20 \mu\text{m}$) is large compared to the transverse extent of the probe beam waist ($w=4.5 \mu\text{m}$), but smaller than the atomic cloud along the propagation direction ($\sim 130 \mu\text{m}$). Measurements are conducted at a peak optical depth per blockade radius $\text{OD}_B \simeq 5$. To suppress dissipative effects, we work at large detuning $\Delta \geq 3\Gamma$ from atomic resonance (Γ is the population decay rate of the $5P_{3/2}$ state, see Fig. 1B), and at a control laser Rabi frequency where the transmission through the medium is the same with and without EIT, but the phase differs significantly (Fig. 1C). Consequently, the transmission hardly varies with probe photon rate (Fig. 1D top), while a strongly rate-dependent phase with a slope of $0.40(7) \text{ rad}\cdot\mu\text{s}$ is observed (Fig. 1D bottom).

To investigate the quantum dynamics of interacting photons, we measure the three-photon correlation function and phase. Since dispersion outside of the atomic medium is negligible, any amplitude and phase features formed inside the nonlinear medium are preserved outside, and can be detected in the form of photon number and phase correlations. The third-order photon correlation function has been measured previously in coupled atom-cavity and quantum dot-cavity systems, as well as in non-classical states of three photons such as the Greenberger-Horne-Zeilinger (GHZ) and ‘N00N’ states [11]. In our approach, we split the light onto three single-photon counting modules. Furthermore, by mixing a detuned local oscillator (LO) into the final beamsplitter, we can also perform a heterodyne measurement in one of the detection arms (Fig. 1A). To connect the observed correlations to the physics of interacting Rydberg polaritons, we consider a state containing up to three photons,

$$|\psi\rangle = |0\rangle + \int dt_1 \psi_1(t_1) |t_1\rangle + \int dt_1 dt_2 \psi_2(t_1, t_2) |t_1, t_2\rangle + \int dt_1 dt_2 dt_3 \psi_3(t_1, t_2, t_3) |t_1, t_2, t_3\rangle, \quad (1)$$

where $|t_1, \dots, t_N\rangle = \frac{1}{N!} a^\dagger(t_1) \cdots a^\dagger(t_N) |0\rangle$, and $a^\dagger(t)$ is the photon creation operator of the time bin mode t . The correlation functions can be related to the wavefunctions as $g^{(2)}(t_1, t_2) = \frac{|\psi_2(t_1, t_2)|^2}{|\psi_1(t_1)|^2 |\psi_1(t_2)|^2}$ and $g^{(3)}(t_1, t_2, t_3) = \frac{|\psi_3(t_1, t_2, t_3)|^2}{|\psi_1(t_1)|^2 |\psi_1(t_2)|^2 |\psi_1(t_3)|^2}$. We refer to the phase $\tilde{\phi}^{(N)}$ of the N -photon wavefunction ψ_N as the N -photon phase, namely, $\tilde{\phi}^{(1)}(t_1) = \text{Arg}[\psi_1(t_1)]$, $\tilde{\phi}^{(2)}(t_1, t_2) = \text{Arg}[\psi_2(t_1, t_2)]$, and $\tilde{\phi}^{(3)}(t_1, t_2, t_3) = \text{Arg}[\psi_3(t_1, t_2, t_3)]$. The N -photon phase is obtained from the phase of the beat note signal on the third detector, conditioned on having observed $N-1$ photons in the other two detectors. The conditional phase relative to N uncorrelated photons, i.e. the nonlinear part of the phase, is denoted as $\phi^{(N)}$ (see Fig 3).

The experimentally measured $g^{(3)}$ function, plotted in Figs. 2A,B, displays a clear bunching feature: the probability to detect three photons within a short time ($\lesssim 25 \text{ ns}$) of one another is six times as likely as for non-interacting photons in a laser beam. The increase at $t_1 = t_2 = t_3$ is accompanied by a depletion region for photons arriving within $\sim 0.7 \mu\text{s}$ of one another, particularly visible along the lines of two-photon correlations $t_i = t_j \neq t_k$ in Fig. 2A: This depletion region is caused by the inflow of probability current towards the center $t_1 = t_2 = t_3$. Figure 2B compares the two-photon correlation function $g^{(2)}(t, t + |\tau|)$ to that for three photons of which two photons were detected in the same time bin, $g^{(3)}(t, t, t + |\tau|)$. The trimer feature (fitted initial slope $\tau_3 = 0.14(2) \mu\text{s}$) is approximately twice narrower than the dimer feature (fitted initial slope $\tau_2 = 0.31(6) \mu\text{s}$), showing that a photon is attracted more strongly to two other photons than to one. Figure 2C illustrates the binding of a third photon to two photons that are detected with a time separation T . If T exceeds the dimer time scale τ_2 , then the third photon binds independently to either photon, while for $T < \tau_2$ the two peaks merge into a single, more tightly bound trimer. This is analogous to the binding of a particle to a double-well potential as the distance between the wells is varied, since the polaritons can be approximately described as interacting massive particles moving at finite group velocity [5].

The dispersive and distance-dependent photon-photon interaction also manifests itself in a large conditional phase shift that depends on the time interval τ between the detection of the conditioning photons (at times $t_1 = t_2 = t$) and the phase measurement on detector D_3 at time t_3 . We observe a conditional phase shift $\phi^{(3)}(t, t, t + |\tau|)$ for the trimer near $\tau = 0$ (Fig. 3A) that is significantly larger than the dimer phase shift $\phi^{(2)}(t, t + |\tau|)$ (Fig. 3B). This confirms the stronger interaction between a photon and a dimer compared to that between one photon and another.

To understand these results quantitatively, we apply an effective field theory (EFT) [20] which describes the low-energy scattering of Rydberg polaritons. This EFT gives us a one-dimensional slow-light Hamiltonian density with a contact interaction.

$$\mathcal{H} = -\hat{\psi}^\dagger \left(i\hbar v_g \partial_z + \frac{\hbar^2}{2m} \partial_z^2 \right) \hat{\psi} - \frac{\hbar^2}{ma} \hat{\psi}^\dagger \hat{\psi}^2, \quad (2)$$

where v_g is the group velocity inside the medium, $m = -\hbar\Omega_c^2/(8\Delta v_g^2)$ is the effective photon mass, $a \approx 17.15(\frac{1}{\text{OD}_B} \frac{\Delta}{\Gamma})^2 r_B$ is the scattering length, Ω_c is the control laser Rabi frequency, and Δ is the one-photon detuning. $\hat{\psi}$ is a quantum field annihilation operator, which corresponds to a photon outside the medium and a Rydberg polariton inside. The bound states can be determined from the Bethe ansatz solution to \mathcal{H} [21, 22], resulting in the correlation functions $g^{(3)}(t_1, t_2, t_3) \propto e^{-\frac{|t_1-t_2|}{a/(2v_g)}} e^{-\frac{|t_2-t_3|}{a/(2v_g)}} e^{-\frac{|t_1-t_3|}{a/(2v_g)}}$ and $g^{(2)}(t_1, t_2) \propto e^{-\frac{|t_1-t_2|}{a/(2v_g)}}$.

In the case $t_1 = t_2 = t$, we find that $g^{(3)}(t, t, t + |\tau|) \propto e^{-2\frac{|\tau|}{a/(2v_g)}}$, implying that the width of three-photon wave-packet (corresponding to $g^{(3)}$) is half that of $g^{(2)}$ for the same experimental conditions, in good agreement with experimental observations. We calculate $a/(2v_g) = 0.32 \mu\text{s}$ for our experimental parameters and find it to be consistent with data (Fig. 2B, dashed lines). Following the quantum quench at the entry of the medium, the initial state is decomposed into the bound state and the continuum of scattering states [5]. In our case, the contribution for scattering states is small near $\tau = 0$, and the bound state dominates the $g^{(3)}$ function in this region. The dimer and trimer binding energies can be estimated as $E_2 = -\frac{\hbar^2}{ma^2} = h \times 0.2 \text{ MHz}$ and $E_3 = 4E_2$ respectively. This binding energy is $\sim 10^{10}$ times smaller than in diatomic molecules such as NaCl and H₂, but is comparable to Feshbach [23] and Efimov [24] bound states of atoms with similar mass m and scattering length a . To further characterize the three-photon bound state, it is instructive to consider the phase ratio $\phi^{(3)}/\phi^{(2)}$. For the bound-state contribution to the conditional phase $\phi^{(3)}(t, t, t)$ ($\phi^{(2)}(t, t)$), the Hamiltonian of Eq.2 predicts a phase that equals the trimer binding energy times the propagation time in the medium. Thus from the bound state contributions, one would expect a ratio $\phi^{(3)}/\phi^{(2)} = 4$, independent of the atom-light detuning Δ . While the observed ratio (Fig. 4B) is approximately constant, it is smaller than 4.

The observed deviation is likely due to the two contributions of comparable magnitude. One correction arises from the scattering states, or equivalently, from the fact that our Rydberg medium ($\sim 130 \mu\text{m}$) is comparable in size to the two-photon bound state ($\sim 280 \mu\text{m}$). For a medium that is short compared to the bound state, one expects the ratio to be 3, consistent with a conventional Kerr medium [25]. The other, more fundamental correction, is due to an interaction that does not arise from pairwise interactions, effectively representing a three-photon force (TPF). Specifically, when all three photons are within one blockade radius of one another, there can be only one Rydberg excitation and the potential cannot exceed the value corresponding to that of two photons [20, 26]. This saturation effect manifests itself as a short-range repulsive TPF which results in a reduction of $\phi^{(3)}/\phi^{(2)}$ below 3 largely due to its effect on the scattering states in the system. The corresponding correction to the bound state is suppressed due to its large size compared to r_B . This explains why the effective TPF has a relatively weak effect on the bunching of $g^{(3)}(|\tau| < 0.2 \mu\text{s})$, which is dominated by the bound state.

To quantitatively understand the effects of the effective TPF, the EFT is modified to include this term (see Supplementary Information). The EFT employs the dipolariton field method to find the values of the effective TPF that match the physical scattering amplitudes in the microscopic model. Using the modified EFT, we compare the results with and without the repulsive TPF, while also taking into account the finite medium (see Fig. 4B). Including this three-photon saturation force allows the phase ratio $\phi^{(3)}/\phi^{(2)}$ to go below 3 and agree with the data. For fully saturated interactions between the polaritons, the interaction potential does not increase with photon number, and the phase ratio should approach 2.

In summary, we have observed photonic solitons in the quantum regime where the soliton shape strongly depends on photon number. These results can be extended along several different directions. First, increasing the length of the medium at constant atomic density would remove the effect of the scattering states through destructive quantum interference

to larger τ and retain only the solitonic bound-state component. Additionally, the strong observed rate dependence of $\phi^{(3)}$ may indicate that larger photonic molecules and photonic clusters could be observed with improved detection efficiency and data acquisition rate. Furthermore, using an elliptical or larger round probe beam and carefully engineering the mass along different directions, the system can be extended to two and three dimensions, possibly permitting the observation of photonic Efimov states [27, 28]. Finally, a threefold increase in the atomic density would render the interaction potential sufficiently deep for a second two/three-photon bound state to appear near zero energy, which should result in resonant photon-photon scattering and a tunable scattering length [29]. The presence of large effective N-body forces in this system opens intriguing possibilities to study exotic many-body phases of light and matter, including self-organization in open quantum systems [30, 31], and quantum materials that cannot be realized with conventional systems.

We thank O. Firstenberg for early stages of this work and S. Choi for discussions. This work has been supported by NSF, NSF CUA, ARO, AFOSR, ARO MURI and Bush Fellowship. AVG and MJG acknowledge support by ARL CDQI, NSF QIS, and NSF PFC at JQI. CC acknowledges funding support from NSF grant PHY-1511696 and Alexander von Humboldt foundation.

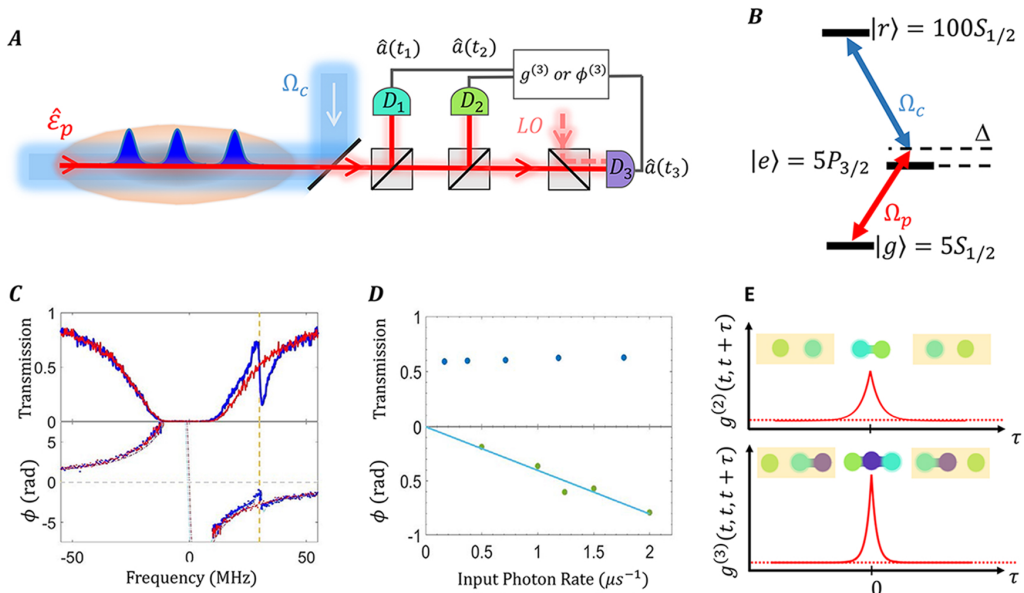


FIG. 1: **A,B**, Setup and atomic level scheme. The atoms are optically pumped into the hyperfine (F) and magnetic (m_F) sublevel $|g\rangle = |5S_{1/2}, F=2, m_F=2\rangle$. The weak coherent probe light is coupled to the Rydberg state $|r\rangle = |100S_{1/2}, m_J=1/2\rangle$, via an intermediate state $|e\rangle = |5P_{3/2}, F=3, m_F=3\rangle$, with linewidth $\Gamma/2\pi = 6.1$ MHz, by means of a counter-propagating control field that is detuned by Δ below the resonance frequency of the upper transition, $|e\rangle \rightarrow |r\rangle$. Strong interactions between probe photons are detected via photon correlations of the transmitted light, which is split onto three single-photon detectors with equal intensities. To perform phase measurements, a local oscillator is mixed into detector D_3 . **C**, Transmission (top) and phase ϕ (bottom) as a function of probe frequency measured at a low ($0.5 \mu\text{s}^{-1}$) input photon rate. ϕ is measured without conditioning on the detection of other photons. The control laser is set at $\Delta/2\pi = 30$ MHz below the $|e\rangle \rightarrow |r\rangle$ transition with Rabi frequency $\Omega_c/2\pi = 10$ MHz. The blue and red data are from measurements with and without control beam, respectively. The blue and red dashed lines in the bottom graph are theoretical expectations. The vertical yellow dashed line marks EIT resonance. **D**, Rate dependence of transmission (top) and unconditional phase (bottom) on two-photon resonance $|g\rangle \rightarrow |r\rangle$, with a one-photon detuning of $\Delta/2\pi = 30$ MHz, and control Rabi frequency $\Omega_c/2\pi = 10$ MHz. While the transmission is rate-independent, the phase is strongly rate dependent (slope is $0.4 \text{ rad}\cdot\mu\text{s}$). **E**, Schematic correlation functions for two (top) and three (bottom) photons as a function of their time separation τ . The attractive interaction leads to photon bunching, with three photons being more tightly bound together than two photons.

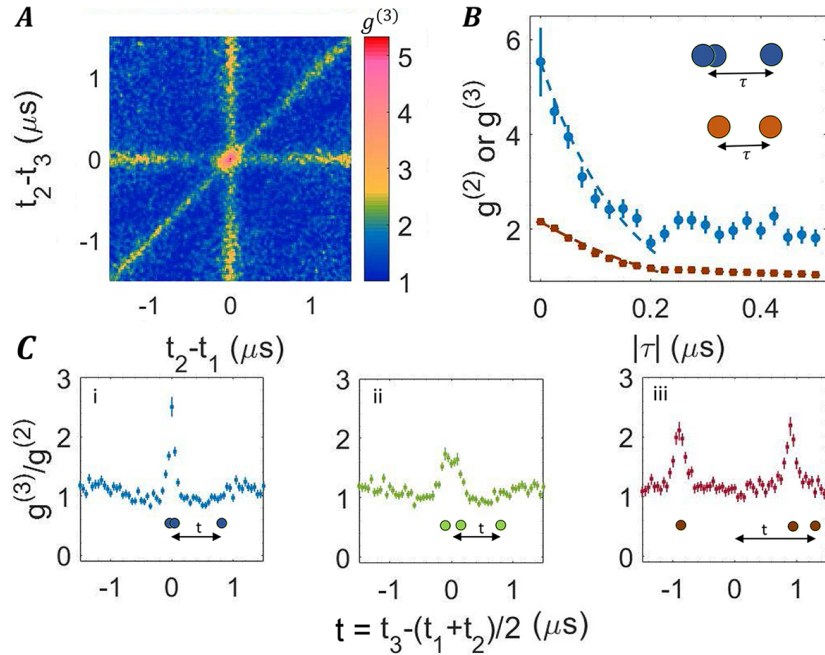


FIG. 2: Photon correlation functions measured at one-photon detuning $\Delta/2\pi = 30$ MHz, control Rabi frequency $\Omega_c/2\pi = 10$ MHz, input photon rate of $1 \mu\text{s}^{-1}$ and on EIT resonance. **A**, Two-dimensional representation of three-photon correlation function $g^{(3)}(t_1, t_2, t_3)$, with t_i being the photon detection time at detector D_i . Three-photon bunching corresponds to the central region, two-photon bunching to the stripes. **B**, $g^{(3)}(t, t, t+|\tau|)$ (blue data points) and $g^{(2)}(t, t+|\tau|)$ (brown data points), with the decay constants calculated from the Bethe Ansatz and scattering length for the bound states $\tau_3^c = 0.16 \mu\text{s}$ and $\tau_2^c = 0.32 \mu\text{s}$ respectively (dashed lines). The calculated exponential decay is scaled to match the initial point of the measured intensity correlation functions. The approximately twice smaller decay length of the three-photon correlation function shows that a photon is more strongly bound to two photons than to one. The fitted slopes for $g^{(3)}$ and $g^{(2)}$ near $\tau = 0$ are $\tau_3 = 0.14(2) \mu\text{s}$ and $\tau_2 = 0.31(6) \mu\text{s}$ respectively (not shown), in agreement with the calculated values. **C**, Three representative plots of $g^{(3)}(t_1, t_2, t_3)/g^{(2)}(t_1, t_2)$ for fixed $T \equiv |t_1 - t_2| = 0 \mu\text{s}$ (i), $T = 0.2 \mu\text{s}$ (ii), and $T = 1.8 \mu\text{s}$ (iii), within a 50 ns window. As we condition on the two photons being further and further away, the sharply decaying $g^{(3)}$ function transitions to a slower decaying $g^{(2)}$ function. For intermediate time separations (ii), there is interference between all states including the dimer and trimer. All permutations of the detectors are used to generate the data in B,C. Error bars in figure indicate one standard deviation (s.d.). Error bars in fitted slope indicate one s.d. of the fit.

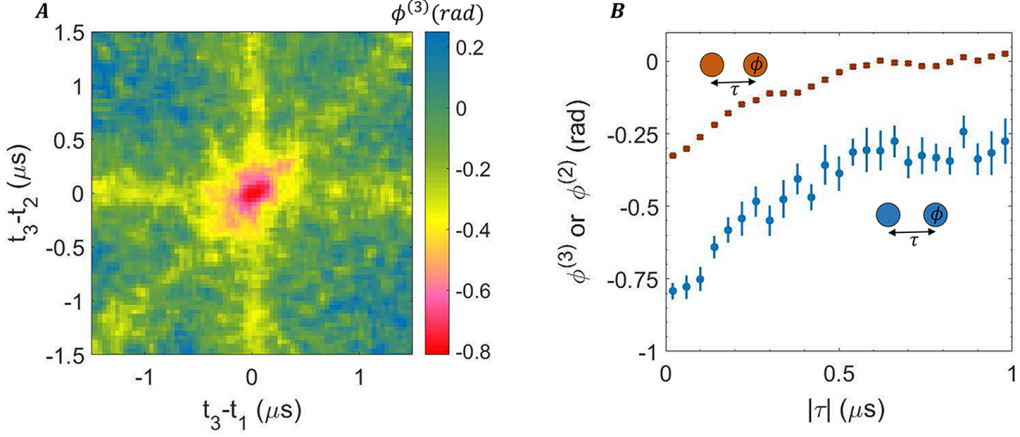


FIG. 3: Nonlinear phase measured under identical conditions as the data in Fig. 2. **A**, Conditional phase $\phi^{(3)}(t_1, t_2, t_3)$, where t_1 and t_2 correspond to photon detection events at detectors D_1 , D_2 , and a heterodyne measurement is performed on detector D_3 at time t_3 . **B**, Diagonal cut $\phi^{(3)}(t, t, t+|\tau|)$ (blue), with the two conditioning probe photons within 40 ns of each other, and $\phi^{(2)}(t, t+|\tau|)$ (brown), showing a larger phase when conditioning on two other near-simultaneous photons ($\phi^{(3)}$) than on one near-simultaneous photon ($\phi^{(2)}$). $\phi^{(N)}$ is referenced to its own average value when all the N photons are too far apart from each other to be correlated. Specifically, $\phi^{(2)}(t_1, t_2) \equiv \tilde{\phi}^{(2)}(t_1, t_2) - (\tilde{\phi}^{(1)}(t_1) + \tilde{\phi}^{(1)}(t_2)) \xrightarrow{|t_1 - t_2| \rightarrow \infty} 0$, and $\phi^{(3)}(t_1, t_2, t_3) \equiv \tilde{\phi}^{(3)}(t_1, t_2, t_3) - (\tilde{\phi}^{(1)}(t_1) + \tilde{\phi}^{(1)}(t_2) + \tilde{\phi}^{(1)}(t_3)) \xrightarrow{|t_i - t_j| \rightarrow \infty, \forall i \neq j} 0$. $\phi^{(3)}$ at large $|\tau|$ asymptotically goes to $\phi^{(2)}(t, t)$, because $\phi^{(3)}(t, t, t+|\tau|) \xrightarrow{|\tau| \rightarrow \infty} \tilde{\phi}^{(2)}(t, t) + \tilde{\phi}^{(1)}(t+|\tau|) - (\tilde{\phi}^{(1)}(t) + \tilde{\phi}^{(1)}(t) + \tilde{\phi}^{(1)}(t+|\tau|)) = \phi^{(2)}(t, t)$. Error bars indicate one standard deviation (s.d.).

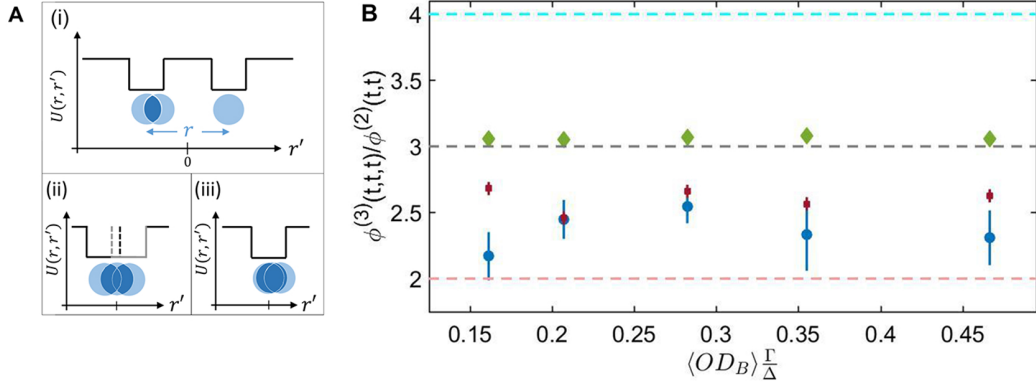


FIG. 4: Effective three-body force for Rydberg polaritons. **A** illustrates the potential (solid black and gray lines) the third photon, at position r' , experiences due to the other two photons, at positions $\pm r/2$. (i) When the two photons are separated by more than twice the blockade radius ($r > 2r_B$), each of them creates its own square potential with a width of $2r_B$; (ii) When the two photons overlap ($r_B < r < 2r_B$), the potential is partially saturated; (iii) When the two photons are within one blockade radius ($r < r_B$), since there can be at most one Rydberg excitation within r_B , the potential is not deeper than that created by one photon. Therefore, we overestimate the attractive potential by considering pairwise interaction only, and a repulsive effective TPF is required to correctly take into account the saturation of the Rydberg blockade. **B**, Measured phase ratio $\phi^{(3)}(t, t) / \phi^{(2)}(t, t)$ (blue) and the EFT predictions (with the TPF in brown; without in green) as a function of $\langle OD_B \rangle \frac{\Gamma}{\Delta}$, where the $\langle \rangle$ refers to the average over the Gaussian profile of the atomic density. The average effective TPF is expected to scale as $\langle OD_B \rangle \frac{\Gamma}{\Delta}$ in units of inverse mass. The control Rabi frequency $\Omega_c/2\pi = \{22, 18, 10, 10, 8\}$ MHz for $\Delta/2\pi = \{54, 42, 30, 24, 18\}$ MHz is chosen such that the transmission is insensitive to the input photon rate (Fig. 1C). We also change the input photon rate $\{0.7, 1, 1, 1.3, 2.5\}$ photons/ μ s to achieve similar data acquisition rates since the losses are larger at smaller detunings. For a fully saturated medium, one expects $\phi^{(3)} / \phi^{(2)} = 2$, as indicated by the pink dashed line; for bound states in a long medium and no effective TPF, one expects $\phi^{(3)} / \phi^{(2)} = 4$, as indicated by the cyan dashed line (see text). EFT results are calculated with parameters from independent measurements, and the two-photon detuning from the EIT resonance is the only parameter varied within the experimental uncertainty to fit the two-photon phase. Error bars indicate one standard deviation (s.d.).

[1] I. H. Deutsch, R. Y. Chiao, and J. C. Garrison, *Phys. Rev. Lett.* **69**, 3627 (1992).

[2] J.-T. Shen and S. Fan, *Phys. Rev. Lett.* **98**, 153003 (2007).

[3] P. Drummond and H. He, *Phys. Rev. A* **56**, R1107 (1997).

[4] Z. Cheng and G. Kurizki, *Phys. Rev. Lett.* **75**, 3430 (1995).

[5] O. Firstenberg, T. Peyronel, Q.-Y. Liang, A. V. Gorshkov, M. D. Lukin, and V. Vuletić, *Nature* **502**, 71 (2013).

[6] P. D. Drummond, R. M. Shelby, S. R. Friberg, and Y. Yamamoto, *Nature* **365**, 307 (1993).

[7] Y. Lai and H. Haus, *Phys. Rev. A* **40**, 854 (1989).

[8] D. Chang, V. Gritsev, G. Morigi, V. Vuletić, M. Lukin, and E. Demler, *Nature Phys.* **4**, 884 (2008).

[9] M. F. Maghrebi, N. Y. Yao, M. Hafezi, T. Pohl, O. Firstenberg, and A. V. Gorshkov, *Phys. Rev. A* **91**, 033838 (2015).

[10] L. Li and A. Kuzmich, *Nature Comm.* **7** (2016).

[11] J.-W. Pan, Z.-B. Chen, C.-Y. Lu, H. Weinfurter, A. Zeilinger, and M. Żukowski, *Rev. Mod. Phys.* **84**, 777 (2012).

[12] I. Friedler, D. Petrosyan, M. Fleischhauer, and G. Kurizki, *Phys. Rev. A* **72**, 043803 (2005).

[13] D. Petrosyan, J. Otterbach, and M. Fleischhauer, *Phys. Rev. Lett.* **107**, 213601 (2011).

[14] A. V. Gorshkov, J. Otterbach, M. Fleischhauer, T. Pohl, and M. D. Lukin, *Phys. Rev. Lett.* **107**, 133602 (2011).

[15] H. Labuhn, D. Barredo, S. Ravets, S. De Léséleuc, T. Macrì, T. Lahaye, and A. Browaeys, *Nature* **534**, 667 (2016).

[16] Y. Dudin and A. Kuzmich, *Science* **336**, 887 (2012).

[17] T. Peyronel, O. Firstenberg, Q.-Y. Liang, S. Hofferberth, A. V. Gorshkov, T. Pohl, M. D. Lukin, and V. Vuletić, *Nature* **488**, 57 (2012).

[18] D. Maxwell, D. J. Szwier, D. Paredes-Barato, H. Busche, J. D. Pritchard, A. Gauguet, K. J. Weatherill, M. P. A. Jones, and C. S. Adams, *Phys. Rev. Lett.* **110**, 103001 (2013).

[19] J. D. Thompson, T. L. Nicholson, Q.-Y. Liang, S. H. Cantu, A. V. Venkatramani, S. Choi, I. A. Fedorov, D. Viscor, T. Pohl, M. D. Lukin, et al., *Nature* **542**, 206 (2017).

[20] M. J. Gullans, J. D. Thompson, Y. Wang, Q.-Y. Liang, V. Vuletić, M. D. Lukin, and A. V. Gorshkov, *Phys. Rev. Lett.* **117**, 113601 (2016).

[21] E. H. Lieb and W. Liniger, *Phys. Rev.* **130**, 1605 (1963).

[22] J. B. McGuire, *Journal of Mathematical Physics* **5**, 622 (1964).

[23] C. Chin, R. Grimm, P. Julienne, and E. Tiesinga, *Rev. Mod. Phys.* **82**, 1225 (2010).

[24] E. Braaten and H.-W. Hammer, *Annals of Physics* **322**, 120 (2007).

[25] P. Bienias and H. P. Büchler, *New Journal of Physics* **18**, 123026 (2016).

[26] K. Jachymski, P. Bienias, and H. P. Büchler, *Phys. Rev. Lett.* **117**, 053601 (2016).

[27] M. J. Gullans, S. Diehl, S. T. Rittenhouse, B. P. Ruzic, J. P. D’Incao, P. Julienne, A. V. Gorshkov, and J. M. Taylor, to be published.

[28] T. Kraemer, M. Mark, P. Waldburger, J. Danzl, C. Chin, B. Engeser, A. Lange, K. Pilch, A. Jaakkola, H.-C. Nägerl, et al., *Nature* **440**, 315 (2006).

[29] P. Bienias, S. Choi, O. Firstenberg, M. F. Maghrebi, M. Gullans, M. D. Lukin, A. V. Gorshkov, and H. P. Büchler, *Phys. Rev. A* **90**, 53804 (2014).

[30] N. Thaicharoen, A. Schwarzkopf, and G. Raithel, *Phys. Rev. Lett.* **118**, 133401 (2017).

[31] P. Schausz, M. Cheneau, M. Endres, T. Fukuhara, S. Hild, A. Omran, T. Pohl, C. Gross, S. Kuhr, and I. Bloch, *Nature* **491**, 87 (2012).

Contents

S1. Microscopic Model	1
S2. Effective Field Theory	2
1. Computing the Three-Body Force	3
2. Comparison Between EFT, Numerical Simulations, and Experimental Data	4
S3. Preparation of N-Body Bound States	6
S4. Binding Energy of the Trimer	7
S5. Finite Rate Corrections to Theory	8
S6. Dissipative Corrections to Theory	9
S7. Methods	10
1. Atom loading and preparation	10
2. Correlation and phase measurement setup	11
References	11

Appendix S1: Microscopic Model

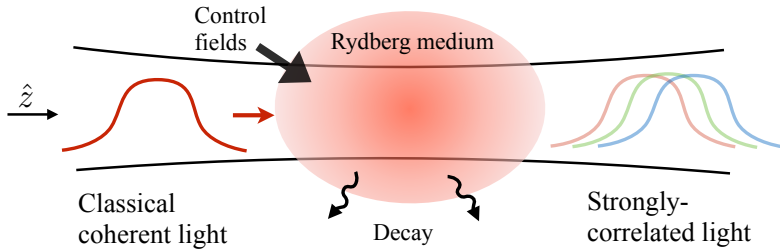


FIG. S1: This experiment can be conceptualized as a multi-particle transport problem whereby a classical coherent pulse of light enters the medium and becomes highly entangled on the output due to strong coherent and dissipative interactions inside the medium.

These experiments can be understood schematically in terms of the multi-particle transport problem illustrated in Fig. S1. A coherent state of light is incident on the quantum nonlinear optical medium formed from Rydberg atoms. Due to the interactions inside the medium, the output light exhibits multi-photon entanglement and correlations. Developing a full theoretical description of the transmitted light field is challenging even in the limit of a few-photons because the photons must be treated as a continuous quantum field. Nevertheless significant simplifications in the theory are possible due to the large separation of scales between the microscopic degrees of freedom and the emergent scales present in the correlations of the output light. We recently developed an effective field theory (EFT) description of this transmission problem by taking advantage of this large separation of scales [S1]. This EFT framework forms the basis of our theoretical analysis of the three-photon transmission problem studied in this work.

As the starting point for our theory we use a continuum description of the problem which first coarse grains over the atomic density to define local continuous quantum fields $\psi_g(z)$, $\psi_p(z)$, and $\psi_s(z)$ for the photons, intermediate atomic excited state, and Rydberg state, respectively. These operators satisfy bosonic commutation relations $[\psi_a(z), \psi_b^\dagger(z')] = \delta_{ab}\delta(z - z')$. In describing the transmission of the photonic field ψ_g , we integrate out the

other transverse propagating photonic degrees of freedom to arrive at a master equation description of the problem ($\hbar = 1$)

$$\dot{\rho} = -i \int dz [\mathcal{H}_0(z) + \mathcal{H}_{\text{int}}(z), \rho] + \gamma \int dz \mathcal{D}[\psi_p(z)]\rho + \gamma_s \int dz \mathcal{D}[\psi_s(z)]\rho, \quad (\text{S1})$$

$$\mathcal{H}_0(z) = \begin{pmatrix} \psi_g(z) \\ \psi_p(z) \\ \psi_s(z) \end{pmatrix}^\dagger \begin{pmatrix} -ic\partial_z & g(z) & 0 \\ g(z) & -\Delta & \Omega/2 \\ 0 & \Omega/2 & -\delta \end{pmatrix} \begin{pmatrix} \psi_g(z) \\ \psi_p(z) \\ \psi_s(z) \end{pmatrix}, \quad (\text{S2})$$

$$\mathcal{H}_{\text{int}} = \int dz' \psi_s^\dagger(z) \psi_s^\dagger(z') V(z - z') \psi_s(z') \psi_s(z), \quad (\text{S3})$$

where $\mathcal{D}[A]\rho = -\{A^\dagger A, \rho\} + 2A\rho A^\dagger$ is a trace-preserving superoperator, \mathcal{H}_0 is the non-interacting Hamiltonian density written in the rotating frame, and \mathcal{H}_{int} is the Rydberg interaction Hamiltonian density. The non-interacting theory is parameterized in terms of the control field Rabi frequency Ω , the halfwidth of the intermediate state γ , the halfwidth of the Rydberg state γ_s , the detuning $\Delta = \omega_{ps} - \omega_c$ between the control field frequency ω_c and the Rydberg-intermediate state transition frequency ω_{ps} , and the two-photon detuning $\delta = \omega_p + \omega_c - \omega_{gs}$ between the sum of ω_c and the input probe frequency ω_p and the ground to Rydberg state transition frequency ω_{gs} . The single-photon Rabi frequency for the probe $g(z)$ is proportional to the square root of the atomic density $n(z)$, with the proportionality constant determined by the resonant optical depth $\text{OD} = \int dz 2[g(z)]^2/\gamma c$. We parameterize the density by a Gaussian profile $n(z) \propto \exp(-z^2/2\sigma_{\text{ax}}^2)$, where σ_{ax} is the RMS axial width of the cloud. Finally, we approximate the Rydberg interactions by their long-range van der Waals tail $V(r) = C_6/r^6$.

An important simplification of this problem is provided for photonic input states with a low photon rate, where the evolution can be described solely in terms of the dynamics induced by the effective non-Hermitian Hamiltonian [S2]

$$\mathcal{H}_{\text{eff}} = \mathcal{H}_0 + \mathcal{H}_{\text{int}} - i\gamma \psi_p^\dagger \psi_p - i\gamma_s \psi_s^\dagger \psi_s. \quad (\text{S4})$$

The decay terms can be incorporated into \mathcal{H}_0 through the replacements $\Delta \rightarrow \Delta + i\gamma$ and $\delta \rightarrow \delta + i\gamma_s$. This approximation relies on the fact that the corrections to the non-Hermitian Hamiltonian evolution from the recycling terms in the master equation, i.e., the so-called “quantum jumps,” are suppressed by higher powers of the polariton density in the medium (see Ref. [S3] for a similar argument applied to a cavity model). Since the experiments are operated in the limit of low polariton densities in the medium, we are justified in neglecting these quantum jump processes. We present a more detailed discussion of these effects in Sec. S6.

Appendix S2: Effective Field Theory

For sufficiently low-energy scattering of two-particles, the dynamics of the Rydberg polaritons are described by the renormalized Lagrangian density [S4]

$$\mathcal{L}_0 = \psi^\dagger \left[i\partial_t + iv_g \partial_z - \frac{1}{2m_0} \partial_z^2 \right] \psi_\mu + \frac{1}{m_0 a} \psi^\dagger \psi^\dagger \psi \psi, \quad (\text{S1})$$

$$v_g = \frac{d\epsilon_D(k)}{dk} \Big|_{k=k_0}, \quad \frac{1}{m_0} = \frac{d^2\epsilon_D(k)}{dk^2} \Big|_{k=k_0}, \quad (\text{S2})$$

where a is the one dimensional scattering length, v_g is the EIT group velocity, and m_0 is the effective mass of the dark state polaritons.

It is well known that, in 1D, Eq. (S1) provides a universal description (i.e., for large values of a) of the low-energy scattering of identical bosons with arbitrarily large particle numbers [S5]. Its eigenstates and energies can be found exactly using the Bethe ansatz and, for $a > 0$, this EFT has one N -body bound state for every N [S6, S7]. The properties of the three-body bound state are discussed in the main text.

For low-energy scattering beyond two-particles, the lowest order correction to this theory is given by a three-body interaction [S8]

$$\mathcal{L}_0 \rightarrow \mathcal{L}_0 - V_3, \quad (\text{S3})$$

$$V_3 = \frac{h_3}{36} \psi^{\dagger 3} \psi^3. \quad (\text{S4})$$

This term, although irrelevant for low-energy, few-body observables under renormalization ($|a| \rightarrow \infty$), has important physical consequences at any finite momentum scale. As discussed in the main text, we can understand the origin of three-body interactions in the Rydberg-EIT system at a qualitative level as arising from the physics of Rydberg blockade. When more than two photons are within a blockade radius from each other, their interaction energy is suppressed due to the blockade effect. This leads to an effective three-body force with the opposite sign from the two-body force as was shown in our recent work [S1] and Ref. [S9]. Although approximate expressions for the three-body interaction were derived in these works, these derivations neglected non-perturbative effects in the renormalization of the microscopic model, which we account for in the section below.

1. Computing the Three-Body Force

In this section, we directly determine the value of the three-body force in the EFT by matching its prediction for the dimer-polariton scattering length to the microscopic model. Here the dimer is the shallow two-body bound state with the binding energy

$$E_D = -\frac{1}{m_0 a^2}. \quad (\text{S5})$$

To better understand the origin of the three-body interaction, we note that the blockaded two-body interaction potential takes the form [S10, S4]

$$U(r) = \frac{\Omega^2}{2\Delta} \frac{1}{1 + r^6/r_b^6}, \quad (\text{S6})$$

where $r_b = (2\Delta C_6/\Omega^2)^{1/6}$ is the blockade radius and we have assumed $\Delta > 0$ and $\Delta \gg \Omega, \gamma$. Represented in momentum space, this potential has a finite weight up to $1/r_b$ before being exponentially suppressed. Near the EIT resonance, the features in the EIT dispersion vary over momentum scales on the order of $g^2/c\Delta$, which implies that, in the small $\phi = g^2 r_b/c\Delta = \text{OD}_b \gamma/\Delta$ regime relevant to these experiments (here OD_b is the optical depth per blockade radius [S11]), the momentum scale associated with the two-body interaction is large compared to the variations in the EIT dispersion (see Fig. S2).

From these observations, we can provide a precise explanation for the origin of the three-body interaction h_3 . The two-body interactions virtually excite the polaritons to the high-momentum regions of the EIT dispersion where the polaritons do not evolve as the massive particles described by Eq. (S1). The quantum fluctuations associated with the virtual excitation of these high-momentum regions can only be included in \mathcal{L}_0 by adding a three-body interaction term. The value of this three-body interaction has to be obtained by matching the predictions of \mathcal{L}_0 to physical observables.

To perform this matching procedure we introduce a modified description of the full microscopic problem that captures much of the physics in the small ϕ regime. In particular, we replace the bare interaction by a contact potential

$$V(r) = \frac{C_6}{r^6} \rightarrow g_2 \delta(r), \quad (\text{S7})$$

which allows the two-body problem to be analytically solved, provided we regularize the theory at the high momentum. Introducing a hard momentum cutoff at the scale Λ , we fix the parameters g_2 and Λ by the matching condition

$$u_0(\omega) = \int dr U(\omega, r) = -\frac{2\pi r_b(\omega)}{3\bar{\chi}(\omega)} e^{i\theta(\omega)/6} = \frac{g_2(\omega)}{1 - g_2(\omega)\bar{\chi}(\omega)\Lambda(\omega)}, \quad (\text{S8})$$

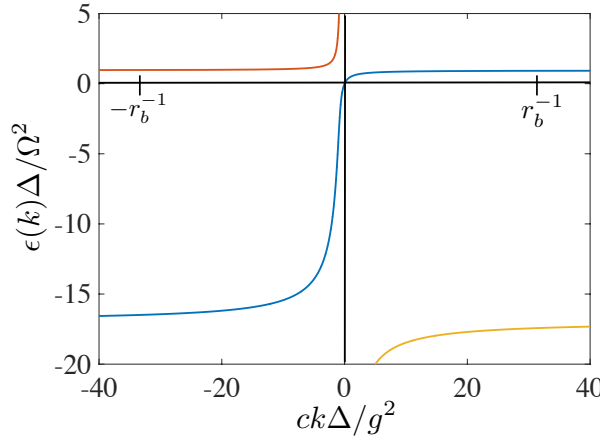


FIG. S2: Scale of blockade radius in the regime $\phi \ll 1$. The effective potential couples momentum up to r_b^{-1} , which includes large regions of the spectrum where the dispersion is not described by that of a massive particle. Here we took $\Omega/2\pi = 10$ MHz, $\Delta/2\pi = 40$ MHz, $\gamma = \gamma_s = 0$, and $g/\Omega = 10^3$.

where we have introduced the parameter $\theta = \arg(-\bar{\chi}C_6)$ to account for the spatial dependence of the inelastic contribution to the effective potential. Note that, in the limit $\Omega \ll |\Delta|$, $\bar{\chi}^{-1} = \omega - \Omega^2/2\Delta$.

Figure S3 shows the value of h_3 in units of the inverse mass, which was obtained from matching the dimer-polariton scattering length in the two theories using numerical solutions of the scattering amplitudes. The self-consistent equations for the scattering amplitudes were obtained using the so-called “dipolariton field method” [S12]. In this approach, we use a Hubbard-Stratonovich transformation to introduce a fictitious field associated with the creation of polariton pairs and, then, solve the two-body scattering problem for this dipolariton field and the bare polariton field. This theoretical technique was first introduced for the three-body problem in the context of Efimov physics [S13]. To regularize UV divergences in our solution for the dimer-polariton scattering amplitude, we take a finite range for the three-body interaction potential

$$V_3^R = \frac{h_3}{36} \int dr' \frac{1}{2\delta r} \theta(\delta r - |r - r'|) d^\dagger(r) d(r) \psi^\dagger(r') \psi(r'), \quad (\text{S9})$$

where $\theta(\cdot)$ is the Heaviside step function and we parameterize $\delta r = \alpha r_b/\phi$ for fixed α . Since $a \approx r_b/\phi^2$, this choice ensures that $\delta r/a \sim \alpha\phi \ll 1$ so that for fixed $\alpha \sim 1$ the three-body potential can be well approximated by a contact interaction at low-momentum. In general, the matching condition depends on the choice of α , however, we find numerically that the scattering length is largely insensitive to this choice.

2. Comparison Between EFT, Numerical Simulations, and Experimental Data

To solve the transmission problem we use a modified version of the EFT that takes into account the spatial inhomogeneity of the atomic density. Most notably, we use a local density approximation (i.e., each parameter is defined in terms of the local value of $g(z)$) and transform into a moving frame through the coordinate transformation [S1]

$$\bar{z} = t - \int_0^z dz' \frac{1}{v_g(z')}, \quad (\text{S10})$$

$$\tau = z, \quad (\text{S11})$$

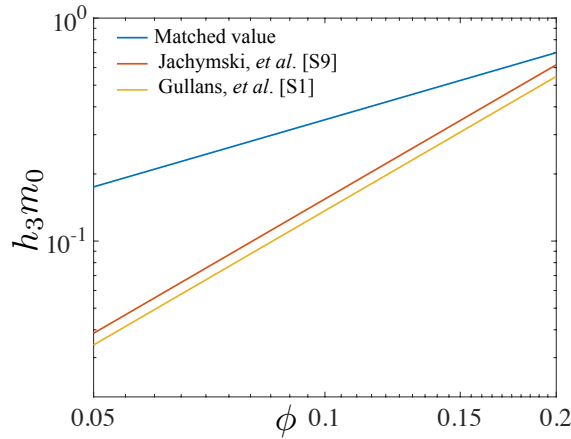


FIG. S3: Dimensionless three-body interaction strength as a function of ϕ in the regime $\Omega \ll \Delta$ for $\alpha = 0.75$.

which transforms the Lagrangian to the form

$$\mathcal{L}_0 = \psi^\dagger \left[i v_g(\tau) \partial_\tau - \frac{\partial_{\bar{z}}^2}{2m_0(\tau) v_g^2(\tau)} \right] \psi + \frac{\psi^{\dagger 2} \psi^2}{m_0(\tau) a(\tau) v_g(\tau)} - \frac{h_3(\tau)}{36 v_g^2(\tau)} \psi^{\dagger 3} \psi^3, \quad (\text{S12})$$

where we have rescaled the field $\psi(z) \rightarrow \psi(\bar{z})/\sqrt{v_g(\tau)}$ such that $[\psi(\bar{z}), \psi^\dagger(\bar{z})] = \delta(\bar{z} - \bar{z}')$ and we have neglected higher-order derivatives involving ∂_τ as their effect is suppressed due to the presence of the linear time derivative. This EFT is a more convenient formulation of the transmission problem because the parameters now depend on “time” τ , which only appears with a single derivative. As a result, this theory can be solved by treating it as a time-dependent Hamiltonian problem. Furthermore, it illustrates that the transmission through the medium can be mapped to a quantum quench, where the duration of the time evolution following the quench is given by the EIT group delay $\tau_d = \int dz [v_g(z)]^{-1}$ [S1, S10, S14].

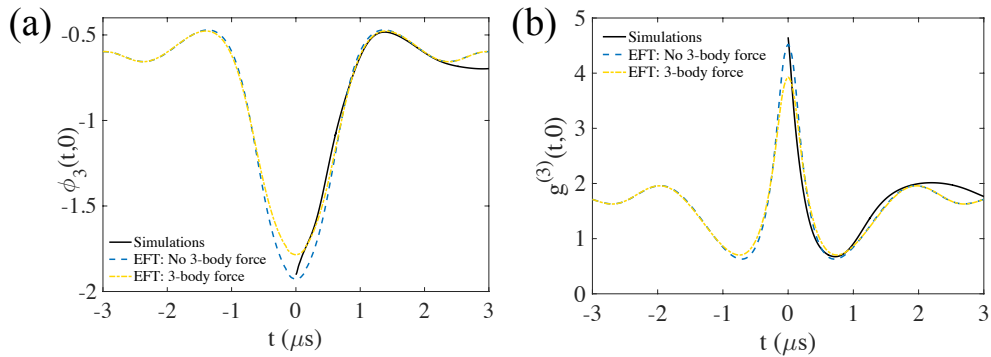


FIG. S4: Comparison between EFT predictions for the two and three photon transmission through a finite medium (see Ref. [S1]) and numerical simulations for (a) the three-photon phase $\phi_3(t, 0)$ and (b) the three-photon amplitude $g^{(3)}(t, 0)$. Here we took parameters similar to the current experiments, but with a uniform density profile of length $144 \mu\text{m}$, a resonant OD=68, $\Omega/2\pi = 5 \text{ MHz}$, $\Delta = 30 \text{ MHz}$, and $r_b = 10 \mu\text{m}$.

In Fig. S4(a-b) we compare the predictions of Eq. (S12) for the transmission through a finite medium to full numerical simulations that account for the microscopic form of the Rydberg interactions [S15]. We see good agreement between the numerics and the EFT at intermediate times. The deviations at short times are due to the breakdown of the low-energy assumption and the deviations at long times arise from the finite length of the

medium [S1]. We use the initial condition outside the medium of a uniform state with unit amplitude. We find that including the three-body interaction improves the agreement with $\phi_3(t, 0)$ at intermediate times. Similar to Fig. 3 in the main text, we see that including the three-photon force reduces the ratio $\phi_3(0, 0)/\phi_2(0)$, where $\phi_2(t)$ is the two-photon phase. Table I shows the ratio $\phi_3(0, 0)/\phi_2(0)$ for the three different models, where we see that including the three-body force is able to account for the deviation of this ratio below 3. Despite the disagreement between the values of $\phi_3(t, 0)$ in the simulations and the EFT at short times seen in Fig. S4, we find that the ratio $\phi_3(t, 0)/\phi_2(t)$ is roughly independent of t near the origin, which justifies the comparison.

In Table II we compare the theoretical predictions from the EFT and the simulations against the measured values of $\phi_3(0, 0)/\phi_2(0)$ from Fig. 4 in the main text. Here $\langle \phi \rangle = \tau_d^{-1} \int dz \phi(z)/v_g(z)$ is the average value of $\phi(z) = \text{OD}_b \gamma / \Delta = g^2(z) r_b / c \Delta$ over the propagation through the medium, weighted by the time spent in each region. As mentioned in the main text, we fit the two-photon detuning δ within the experimental uncertainty $\delta/2\pi = 0.0 \pm 0.5$ MHz by matching the measured value of $\phi_2(0)$ to the simulations, while all other parameters are determined from independent measurements without fitting. Although $\phi_2(0)$ and $\phi_3(0, 0)$ are sensitive to the precise value of δ , we find that the theoretical prediction for the ratio $\phi_3(0, 0)/\phi_2(0)$ varies by less than 5 % when varying δ within the experimental uncertainty. We see that the EFT with the three-body force gives good agreement with both the data and the simulations, while we can clearly rule out the EFT without the three-body force.

Model	$\phi_3(0, 0)/\phi_2(0)$
Simulations	2.90
EFT: No 3-body force	3.13
EFT: 3-body force	2.80

TABLE I: Comparison for the prediction of the phase ratio near zero time delay between different models for parameters as in Fig. S4.

$\langle \phi \rangle = \langle \text{OD}_b \rangle \gamma / \Delta$	0.16	0.21	0.28	0.36	0.47
Measured $\phi_3(0, 0)/\phi_2(0)$	$2.17 \pm .14$	$2.32 \pm .12$	$2.57 \pm .10$	$2.56 \pm .15$	$2.56 \pm .11$
EFT: 3-body force	2.68	2.46	2.66	2.57	2.63
Simulations	2.77	2.66	2.72	2.63	2.60
EFT: No 3-body force	3.06	3.05	3.07	3.08	3.06
Fitted δ (2 π -MHz)	0.6	0.6	0	-0.2	-0.4

TABLE II: Comparison of measured $\phi_3(0, 0)/\phi_2(0)$ presented in Fig. 4B of the main text to predictions from EFT with and without the three-body force and the simulations [S15]. We took an inhomogeneous Gaussian density profile with $\sigma_{\text{ax}} = 35$ μm , δ as shown (obtained from fitting the measured value of $\phi_2(0)$ to the simulations), and other parameters as given in the main text.

Appendix S3: Preparation of N -Body Bound States

In this section we present a general argument that the propagation through the medium leads to the formation of an N -body bound state near zero time delay between the polaritons. We first consider the two-body problem in a uniform medium. Defining the center of mass $R = (z_1 + z_2)/2$ and relative $r = z_1 - z_2$ coordinates for the two polaritons, we expand the wavefunction in the eigenbasis of the EFT given in Eq. (S1) [S10]

$$\psi(t, R, r) = c_b e^{-|r|/a - iE_D t} + \int_0^\infty \frac{dq}{2\pi} c_q \psi_q(r) e^{-iq^2 t/m_0}, \quad (\text{S1})$$

where the first term is the dimer wavefunction, $\psi_q(r) = (e^{iq|r|} + b_q e^{-iq|r|})/\sqrt{2}$ is the wavefunction for the two-body scattering states, $b_q = (iaq + 1)/(iaq - 1)$, and we work in the center of mass frame so that $\partial_R \psi = 0$. The coefficients c_b and c_q are determined by initial conditions.

For a long medium, we can find the transmission analytically for $|r|/a \ll \sqrt{|E_D t|}$ using a saddle point expansion

$$\psi(t, R, r) \approx c_b e^{-|r|/a - i E_D t} + O(|E_D t|^{-1/2}), \quad (\text{S2})$$

where the second term is due to the contribution from scattering states. The condition to neglect the second term for the transmitted light is

$$\tau_d |E_D| \approx 4\phi^2 \text{OD} \gamma / \Delta \gg 1, \quad (\text{S3})$$

where τ_d is the EIT group delay defined in Sec. S2.2. From this analysis we see that the dispersive nature of the scattering states results in the bound state dominating the transmission near the origin in the off-resonant, high OD limit.

To see how this argument generalizes to $N > 2$, we move to a relative coordinate system r_1, \dots, r_{N-1} (defined as any set of coordinates orthogonal to the center of mass coordinate $R = \sum_i z_i/N$). The general form for the evolution in the center of mass frame is given by

$$\psi(t, R, \mathbf{r}) = c_b \psi_b(\mathbf{r}) e^{-i E_N t} + \int \frac{dq}{2\pi} c_{bq} \psi_{bq}(\mathbf{r}) e^{-i E_{N-1} t - iq^2 t / 2m_0} + \dots, \quad (\text{S4})$$

where ψ_b is the wavefunction for the N -body bound state, $\psi_{bq}(\mathbf{r})$ is the wavefunction for a combined $(N-1)$ -body bound state and a scattering state with relative momentum q , etc. Similar to the two-body problem, we can see that all contributions to ψ besides ψ_b will dephase with each other. As a result, the transmission is dominated by the bound state near the origin.

For the experiments studied in this work, $|E_N| \gtrsim \tau_d^{-1}$, therefore, it is important to also take into account the contributions from the scattering states in solving the transmission problem. To include these contributions when modeling the experiments, we perform numerical simulations of the two and three-photon wavefunction propagation equations derived from the EFT in Eq. (S12) including the inhomogeneous density profile.

Appendix S4: Binding Energy of the Trimer

Using the EFT with the matched value of h_3 , we can find the binding energy of the trimer E_T from the eigenvalue equation for the three-body bound states [S8, S12]

$$B_p = \int \frac{dq}{2\pi} \left(\frac{1}{m_0 E_T - q^2 - p^2 - pq} + \frac{h_3 m_0 a^2}{36} \right) \frac{-4}{a - \sqrt{\frac{1}{3q^2/4 - m_0 E_T}}} B_q, \quad (\text{S1})$$

where B_p is related to the wavefunction of the three-body bound state. For $h_3 = 0$, the binding energy is given by the Bethe ansatz solution

$$E_T^0 = -\frac{4}{m_0 a^2}. \quad (\text{S2})$$

We define $\delta E_T = E_T - E_T^0$ as the correction to the binding energy due to the three-body interaction. Figure S5 shows the comparison between δE_T and $|h_3|$ as a function of the interaction parameter ϕ . We work in energy units of $\Omega^2/4\Delta$ and momentum units of $g^2/c\Delta$, which are natural units for the transmission problem because, in these units, $v_g = 1$ and $m_0 = -2$ on EIT resonance. We see that δE_T goes to zero much faster with decreasing ϕ than $|h_3|$. This difference arises because, as the interactions become weaker, the trimer becomes more weakly bound and the three particles feel a weaker effect from the three-body interactions. This observation explains why the three-photon force shows up more strongly in $\phi_3(0, 0)/\phi_2(0)$, which scales as $h_3 m_0$, than in the slope of $g^{(3)}(t, t + \tau)$, which is approximately equal to $\sqrt{|m_0 E_T|}$.

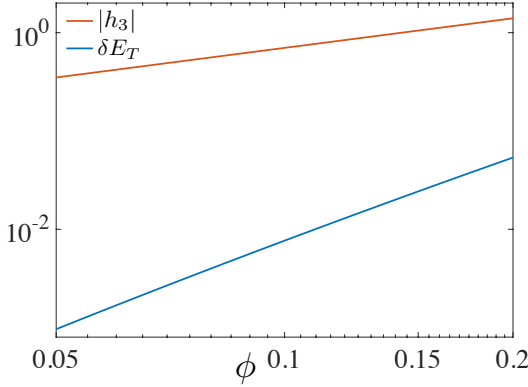


FIG. S5: Three-body interaction $|h_3|$ from Fig. S3 and the correction to the trimer binding energy δE_3 in energy units of $\Omega^2/4\Delta$ and momentum units of $g^2/c\Delta$.

Appendix S5: Finite Rate Corrections to Theory

The correlation functions analyzed above were taken with respect to the vacuum. In the experiment, the input state is a coherent state, which implies that N -particle correlation functions contain contributions from higher and lower particle-number manifolds. In the limit of a long coherent state pulse with a finite photon rate R , we now evaluate these corrections perturbatively in the normalized polariton density $R\tau_{\text{int}}$. Here $\tau_{\text{int}} \sim \tau_d$ is defined as the relative time difference over which the correlation functions do not factorize.

We write the input state as

$$e^{\alpha^2/2}|\mathcal{E}\rangle = |0\rangle + \alpha|1\rangle + \frac{\alpha^2}{\sqrt{2!}}|2\rangle + \frac{\alpha^3}{\sqrt{3!}}|3\rangle + \dots, \quad (\text{S1})$$

where

$$|n\rangle = \frac{(a^\dagger)^n}{\sqrt{n!}}|0\rangle, \quad a^\dagger = \frac{1}{\sqrt{T}} \int dz \mathcal{E}(z) \psi_g^\dagger(z). \quad (\text{S2})$$

Here $\mathcal{E}(z)$ is our input mode which we take to be a long uniform pulse of unit amplitude and duration T from $z = 0$ to $z = T$ (c=1). We write the output as

$$\begin{aligned} e^{\alpha^2/2}|\mathcal{E}\rangle &= |0\rangle + \sqrt{R} \int dz \mathcal{E}_1(z) \psi_g^\dagger(z) |0\rangle + \frac{R}{2} \int dz_1 dz_2 \mathcal{E}_2(z_1, z_2) \psi_g^\dagger(z_1) \psi_g^\dagger(z_2) |0\rangle \\ &\quad + \frac{R^{3/2}}{6} \int dz_1 dz_2 dz_3 \mathcal{E}_3(z_1, z_2, z_3) \psi_g^\dagger(z_1) \psi_g^\dagger(z_2) \psi_g^\dagger(z_3) |0\rangle + \dots, \end{aligned} \quad (\text{S3})$$

where the input photon rate is $R = \alpha^2/T$ and we define g_n and ϕ_n via

$$\mathcal{E}_n(z_1, \dots, z_n) = \sqrt{g_n(z_1, \dots, z_n)} e^{i\theta_n(z_1, \dots, z_n)}. \quad (\text{S4})$$

Notice that g_n and θ_n are different from the measured $g^{(n)}$ and ϕ_n because of the rate-dependent corrections. Neglecting dissipation leads to the normalization condition

$$e^{\alpha^2} = e^{\alpha^2} \langle \mathcal{E} | \mathcal{E} \rangle = 1 + R \int dz_1 g_1(z_1) + \frac{R^2}{2} \int dz_1 dz_2 g_2(z_1, z_2) + \dots, \quad (\text{S5})$$

which requires the identity

$$\int d^n z [g_n(z_1, \dots, z_n) - 1] = 0. \quad (\text{S6})$$

One can show that including the decay rates in the effective Hamiltonian gives the leading order contribution to this integral on the order of $(\gamma/\Delta)\tau_{\text{int}}^n$.

These identities allow us to prove that g_n converges to $g^{(n)}$ in the limit of vanishing input rate $R\tau_{\text{int}} \rightarrow 0$. For example, for g_2 we find

$$\begin{aligned} g^{(2)}(z_1, z_2) &= \frac{1}{R^2} \langle \mathcal{E} | \psi_g^\dagger(z_1) \psi_g^\dagger(z_2) \psi_g(z_2) \psi_g(z_1) | \mathcal{E} \rangle \\ &= e^{-\alpha^2} [g_2(z_1, z_2)(1 + \alpha^2 + \dots) + R \int dz [g_3(z_1, z_2, z) - g_2(z_1, z_2)] + \dots], \end{aligned} \quad (\text{S7})$$

Collecting all terms that are zeroth order in $R\tau_{\text{int}}$, we recover $g_2(z_1, z_2)$. In the limit $\Delta \gg \gamma$, this analysis also gives access to the first order correction in $R\tau_{\text{int}}$, which takes the general form

$$\begin{aligned} g^{(n)}(\tau_1, \dots, \tau_{n-1}) &= g_n(\tau_1, \dots, \tau_{n-1}) \\ &\quad + R \int d\tau (g_{n+1}(\tau_1, \dots, \tau_{n-1}, \tau) - g_n(\tau_1, \dots, \tau_{n-1})). \end{aligned} \quad (\text{S8})$$

For the single-photon phase, we can follow similar arguments to find

$$\frac{1}{\sqrt{R}} \langle \mathcal{E} | \psi_g(z) | \mathcal{E} \rangle = e^{i\theta_1} + R \int d\tau (\sqrt{g_2(\tau)} e^{i(\theta_2(\tau) - \theta_1)} - e^{i\theta_1}) + O(R^2 \tau_{\text{int}}^2), \quad (\text{S9})$$

and, generalizing to ϕ_n ,

$$\begin{aligned} \frac{1}{R^{n-1/2}} \langle \mathcal{E} | \psi_g^\dagger(z_1) \cdots \psi_g^\dagger(z_{n-1}) \psi_g(z) \psi_g(z_{n-1}) \cdots \psi_g(z_1) | \mathcal{E} \rangle &= \mathcal{E}_{n-1}^*(z_1, \dots, z_{n-1}) \mathcal{E}_n(z_1, \dots, z_{n-1}, z) \\ &\quad + R \int dz' [\mathcal{E}_n^*(z', z_1, \dots, z_{n-1}) \mathcal{E}_{n+1}(z', z_1, \dots, z_{n-1}, z) \\ &\quad - \mathcal{E}_{n-1}^*(z_1, \dots, z_{n-1}) \mathcal{E}_n(z_1, \dots, z_{n-1}, z)]. \end{aligned} \quad (\text{S10})$$

Using these formulas, we have explicitly evaluated the rate dependent corrections to ϕ_2 and ϕ_3 by numerically solving the four-photon transmission problem within the EFT. The results are shown in Fig. S6. For this data set ($\Delta/2\pi = 30$ MHz), the experiments were performed at a rate near 1 photon/ μ s. In this regime, the rate dependent corrections to the phase ratio are on the order of a few percent. This mostly rules out the rate dependent corrections as an explanation for the deviation of the phase ratio from three observed in the experiment. We find similar results for the other data sets. In Fig. 4B of the main text we compare the zero-rate predictions of the EFT to the experimentally measured values of $\phi_3(0, 0)/\phi_2(0)$. In Fig. 4B of the main text we compare the zero-rate predictions of the EFT to the experimentally measured values of $\phi_3(0, 0)/\phi_2(0)$.

Appendix S6: Dissipative Corrections to Theory

At large single-photon detunings Δ the dominant decay is due to the finite decoherence rate γ_s of the Rydberg state. Experimentally we observe that the single-photon transmission through the medium is between 50 % and 90 %. Although we include the decay terms in the non-Hermitian Hamiltonian evolution, this large background decay inside the medium raises the question of whether we are justified in neglecting the recycling terms in the master equation. As was argued in Sec. S1, this approximation is indeed justified at sufficiently low polariton densities. More precisely, we find the requirement to neglect the recycling terms is given by $\gamma_s \tau_d R \tau_{\text{int}} \ll 1$. This condition is well satisfied for the experiment even when $\gamma_s \tau_d \sim 1$, which justifies our theoretical approach.

We do not give a detailed proof of this result here, but note that this scaling can be understood intuitively because $\gamma_s \tau_d$ is the expected number of decay events, or “quantum jumps,” per photon during the transmission through the medium, while $R\tau_{\text{int}}$ is the probability of having a second photon within the interaction range of the first when the quantum jump occurs, i.e., the normalized polariton density. Thus, under the condition $\gamma_s \tau_d R \tau_{\text{int}} \ll 1$, the

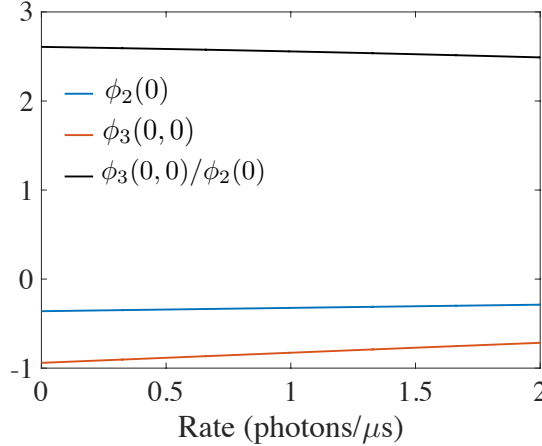


FIG. S6: Rate dependent corrections within the EFT for parameters from the 30 MHz data set. The experiment for this data set was performed at a rate of 1 photon/μs.

quantum jumps typically happen when there are no other polaritons nearby with which to interact. In this case, the interacting correlation functions will have a small contribution from quantum jump events from higher excitation number manifolds.

The role of quantum jumps associated with other loss processes inside the medium requires a separate treatment from the Rydberg decay because these effects appear in the polariton dynamics as momentum or frequency dependent loss (e.g., an imaginary mass term). In this case, the argument above does not apply because, for a long uniform pulse that has reached steady state inside the medium, these loss processes are always correlated with interactions between the polaritons. As a result, these quantum jump events do not average out when evaluating interacting correlation functions. It is not difficult to show, however, that these corrections are suppressed as the product of two small parameters $R\tau_{\text{int}}$ and γ/Δ , which justifies our neglect of these quantum jump processes.

Appendix S7: Methods

1. Atom loading and preparation

The ^{87}Rb atoms are loaded from a 3D magneto-optical trap (MOT) into a 1064 nm crossed dipole trap. The dipole trap is modulated with a period of 40 μs and 80 % duty cycle. A $\sim 6 \mu\text{s}$ long probe pulse is sent to the atomic cloud while the dipole trap is off to avoid inhomogeneous AC Stark shift and the anti-trapping of the Rydberg atoms. The modulation of the trap and therefore the measurements last for 120 ms before a new atomic cloud is loaded. The average resonant optical depth along the atomic cloud is 36. The root-mean-square (rms) length of the medium is 32 μm . The atoms are optically pumped into the hyperfine (F) and magnetic (m_F) sublevel $|g\rangle = |5S_{1/2}, F = 2, m_F = 2\rangle$. The weak coherent probe light is coupled to the Rydberg state, via an intermediate state $|e\rangle = |5P_{3/2}, F = 3, m_F = 3\rangle$, of linewidth $\Gamma/2\pi = 6.1$ MHz, by means of a counter-propagating control field that is detuned by Δ below the resonance frequency of the upper transition, $|e\rangle \rightarrow |r\rangle = |100S_{1/2}, m_J = 1/2\rangle$, in the presence of a 3 G magnetic field along the long axis of the cloud. Probe and control counter-propagate along the quantization axis. The blockade radius r_B defined as $(C_6 \frac{4|\Delta|}{\Omega_c^2})^{\frac{1}{6}}$ is 20 μm , where $C_6/\hbar = 2\pi \times 56.4$ THz·(μm^6) is the van der Waals coefficient and $\Delta = 30$ MHz is the one-photon detuning.

2. Correlation and phase measurement setup

In Fig. 1A of the main text, the first two beam splitters are polarizing beam splitters (PBS), and the last one is a 8:92 pellicle beam splitter to minimize loss of the probe photons. There are polarization optics (not shown in the figure) before the first PBS to clean up the polarization of the probe, after which a half-wave plate is placed before each PBS to balance the detection rates on the three detectors.

We obtain the phase by performing a heterodyne measurement by mixing the transmitted probe light with a local oscillator (LO) at detector D_3 as shown in Fig. 1A. The LO is blue detuned by 79 MHz from the probe laser and this frequency difference is generated by an acousto-optic modulator (AOM). Afterwards, the two beams are sent through their own optical fibers. In order to take out the phase fluctuations caused by the fibers, we interfere the probe and LO, and trigger the single-photon detectors with the beatnote, which serves as a time zero for each probe pulse. Unlike the probe, the LO does not propagate through the atomic cloud, causing an additional phase drift on a time scale of tens of milliseconds. We keep track of the overall phase drift by fitting the unconditional phase for each time interval of ~ 10 ms. The interpolation of this time-dependent unconditional phase is added to each detection event on detector D_3 (phase measurement) to enable averaging over hours for the conditional phase measurements. Since we only detect one output port of the pellicle beam splitter, the intensity noise cannot be canceled as in a balanced detection. Therefore, the LO counts is kept about four times of that of the probe on detector D_3 .

To produce the unconditional phase measurement in Fig. 1C of the main text, we modulate probe-dipole trap for 5 ms. The sequence is adjusted such that during this 5 ms measurement time, the average optical depth is the same as a usual sequence. After that, we shut off the dipole trap and allow the atomic cloud to expand for 1 ms. We then measure the unconditional phase for 4 ms and use it as the phase reference.

The rate-dependent $\phi^{(1)}$ in Fig. 1D of the main text is generated by alternating relatively strong and weak (input photon rate of $0.5 \mu\text{s}^{-1}$) pulses. The weak pulse serves as the phase reference, and a constant offset is applied to all the points such that the linear fit crosses the origin.

By conditioning on detecting two probe photons at time t_1 and t_2 , and performing a phase measurement at time t_3 , we directly measure $\tilde{\phi}^{(3)}(t_1, t_2, t_3) - \tilde{\phi}^{(2)}(t_1, t_2) - \tilde{\phi}_{\text{ref}}^{(3)}$. From the same data, by conditioning on detecting one probe photon, we obtain $\tilde{\phi}^{(2)}(t_1, t_2) - \tilde{\phi}^{(1)}(t_1) - \tilde{\phi}_{\text{ref}}^{(2)}$, where $\tilde{\phi}_{\text{ref}}^{(N)}$ denotes the phase reference of the directly measured phase conditioning on detecting $N-1$ probe photons. We can use the local unconditional phase when the phase measurement is performed as the reference, as in Fig. S7, namely, $\tilde{\phi}_{\text{ref}}^{(3)} = \tilde{\phi}^{(1)}(t_3)$ and $\tilde{\phi}_{\text{ref}}^{(2)} = \tilde{\phi}^{(1)}(t_2)$. For uncorrelated photons, N -photon phase can be written as the sum of the one-photon phase, e.g. $\tilde{\phi}^{(3)}(t_1, t_2, t_3) \xrightarrow{|t_i - t_j| \rightarrow \infty, \forall i \neq j} \tilde{\phi}^{(1)}(t_1) + \tilde{\phi}^{(1)}(t_2) + \tilde{\phi}^{(1)}(t_3)$. Therefore, at large $|\tau|$, both conditional phases in Fig. S7 are expected to go to 0. However, there is small disagreement between the unconditional and the conditional phase with well separated photons. The conditional phases vary at a time scale of a few tens of microseconds, much slower than the bound state physics. Additionally, the mismatch is only less than 20 % of the phase of the concurrent photons. Therefore, we do not believe the phase offset at large τ to have significant impact on our main results.

In the main text, on the other hand, we use its own average value when the two photons are far away from each other as the phase reference $\tilde{\phi}_{\text{ref}}^{(2)}$. $\tilde{\phi}_{\text{ref}}^{(3)}$ includes both the phase of the uncorrelated photons and the phase conditioning on detecting one probe photon, namely, $\tilde{\phi}_{\text{ref}}^{(3)} = \tilde{\phi}^{(1)}(t_3) - (\tilde{\phi}^{(2)}(t_1, t_2) - \tilde{\phi}^{(1)}(t_1) - \tilde{\phi}_{\text{ref}}^{(2)})$. Assuming all detectors are interchangeable, this leads to $\tilde{\phi}^{(3)}(t_1, t_2, t_3) - (\tilde{\phi}^{(1)}(t_1) + \tilde{\phi}^{(1)}(t_2) + \tilde{\phi}^{(1)}(t_3))$, defined as $\phi^{(3)}(t_1, t_2, t_3)$ in the main text.

[S1] M. J. Gullans, J. D. Thompson, Y. Wang, Q.-Y. Liang, V. Vuletić, M. D. Lukin, and A. V. Gorshkov, Phys. Rev. Lett. **117**, 113601 (2016).

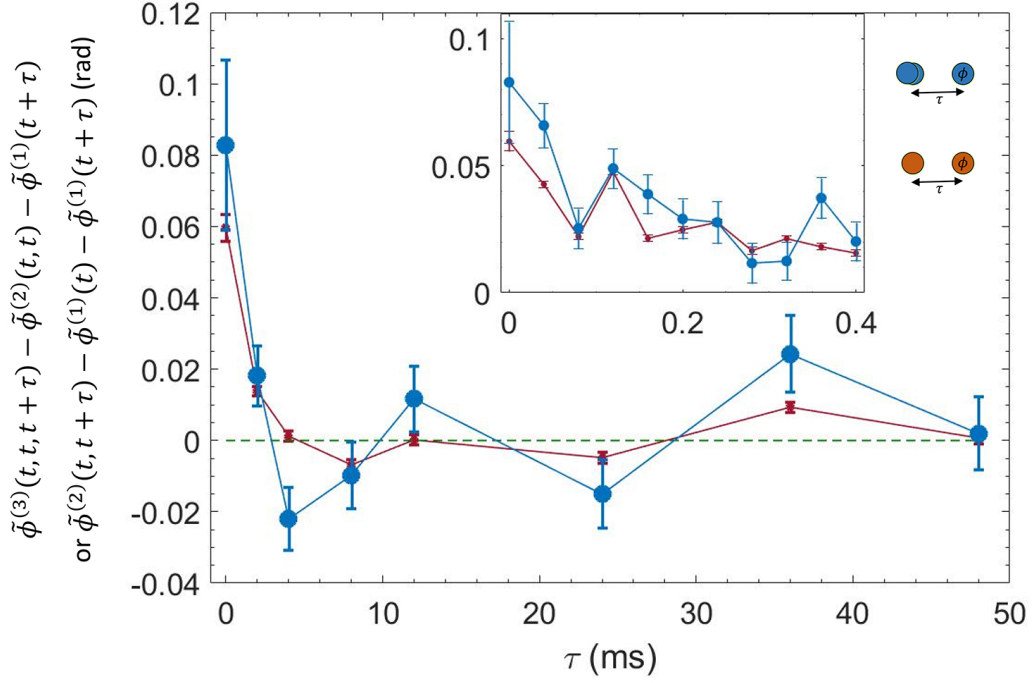


FIG. S7: The long range behavior of the conditional phase referenced to the local unconditional phase. The blue and brown data represent $\tilde{\phi}^{(3)}(t, t, t + \tau) - \tilde{\phi}^{(2)}(t, t) - \tilde{\phi}^{(1)}(t + \tau)$ (rad) and $\tilde{\phi}^{(2)}(t, t + \tau) - \tilde{\phi}^{(1)}(t) - \tilde{\phi}^{(1)}(t + \tau)$ (rad), respectively. The inset shows the same quantities at a shorter time scale. These data with τ much longer the probe pulse ($\sim 6\mu\text{s}$) are generated by taking detection events from different pulses. Data is the same as in Fig. 3 of the main text.

- [S2] T. Peyronel, O. Firstenberg, Q.-Y. Liang, S. Hofferberth, A. V. Gorshkov, T. Pohl, M. D. Lukin, and V. Vuletić, *Nature* **488**, 57 (2012).
- [S3] H. Carmichael, R. Brecha, and P. Rice, *Opt. Commun.* **82**, 73 (1991).
- [S4] P. Bienias, S. Choi, O. Firstenberg, M. F. Maghrebi, M. Gullans, M. D. Lukin, A. V. Gorshkov, and H. P. Büchler, *Phys. Rev. A* **90**, 053804 (2014).
- [S5] S. K. Adhikari, T. Frederico, and I. D. Goldman, *Phys. Rev. Lett.* **74**, 487 (1995).
- [S6] E. H. Lieb and W. Liniger, *Phys. Rev.* **130**, 1605 (1963).
- [S7] J. B. McGuire, *J. Math. Phys.* **5**, 622 (1964).
- [S8] E. Braaten and H. W. Hammer, *Phys. Rep.* **428**, 259 (2006).
- [S9] K. Jachymski, P. Bienias, and H. P. Büchler, *Phys. Rev. Lett.* **117**, 053601 (2016).
- [S10] O. Firstenberg, T. Peyronel, Q.-Y. Liang, A. V. Gorshkov, M. D. Lukin, and V. Vuletić, *Nature* **502**, 71 (2013).
- [S11] A. V. Gorshkov, J. Otterbach, M. Fleischhauer, T. Pohl, and M. D. Lukin, *Phys. Rev. Lett.* **107**, 133602 (2011).
- [S12] M. J. Gullans *et al.* in preparation.
- [S13] P. F. Bedaque, H.-W. Hammer, and U. van Kolck, *Phys. Rev. Lett.* **82**, 463 (1999).
- [S14] P.-É. Larré and I. Carusotto, *Phys. Rev. A* **92**, 043802 (2015).
- [S15] M. J. Gullans, PhD Thesis, Harvard University, Cambridge, MA (2013).